A three-dimensional model and numerical simulation regarding thermoseed mediated magnetic induction therapy conformal hyperthermia

Heng Wang, Jianan Wu, Zihan Zhuo and Jintian Tang*
Key Laboratory of Particle Technology and Radiation Imaging of Ministry of Education, Department of Engineering Physics, Tsinghua University, Beijing, China

Abstract. In order to ensure the safety and effectiveness of magnetic induction hyperthermia in clinical applications, numerical simulations on the temperature distributions and extent of thermal damage to the targeted regions must be conducted in the preoperative treatment planning system. In this paper, three models, including a thermoseed thermogenesis model, tissue heat transfer model, and tissue thermal damage model, were established based on the four-dimensional energy field, temperature field, and thermal damage field distributions exhibited during hyperthermia. In addition, a numerical simulation study was conducted using the Finite Volume Method (FVM), and the accuracy and reliability of the magnetic induction hyperthermia model and its numerical calculations were verified using computer simulations and experimental results. Thus, this study promoted the application of computing methods to magnetic induction therapy and conformal hyperthermia, and improved the accuracy of the temperature field and tissue thermal damage distribution predictions.

Keywords: Magnetic induction hyperthermia, numerical simulation, tissue thermal damage, FVM

1. Introduction

Magnetic induction hyperthermia was first proposed as a treatment for tumors by Gilchfist in 1960 [1], who demonstrated that when magnetic particles are selectively placed in tumor regions and irradiated with an alternating magnetic field, local hyperthermia can be achieved. However, in order to prevent irreversible thermal damage to normal tissues, an appropriately effective temperature must be applied to the tumor. Therefore, preoperative temperature simulation and treatment plan preparations are necessary.

Studies concerning hyperthermia planning systems were initiated in the 1970s [2,3] and developed in the 1980s and 1990s [4–6]. In 2007, the Magforce Company in Berlin, Germany began to develop the planning system NanoPlan and apply it to clinical trials [7,8]; in 2011, the Dutch scholar Linthorst et al. established a 3D model for epidermal hyperthermia planning [9]. In addition, in 2012, Di Barba et al. proposed an optimization method for treatment planning using finite element analysis [10], and in

---

*Corresponding author: Jintian Tang, Key Laboratory of Particle Technology and Radiation Imaging of Ministry of Education, Department of Engineering Physics, Tsinghua University, Beijing 100084, China. Tel.: +86 010 62796769; Fax: +86 010 62789237; E-mail: tangjt@mail.tsinghua.edu.cn.

2013, Paulides et al. from the University of California conducted a study to compare and optimize the simulation techniques of existing hyperthermia [11]. Furthermore, in 2014, Stigliano et al. conducted experiments in order to validate the existing magnetic induction treatment planning system models [12]. In recent years, research concerning magnetic induction hyperthermia planning has progressed. However, the multi-dimensional thermal field calculation models and numerical simulation methods of the existing hyperthermia planning systems cannot accurately predict thermal doses.

Thus, in order to accurately predict thermal doses, a 3D model was established and numerical calculations and simulations based on FVM were conducted. With these developments, temperature field and thermal tissue damage distributions could be calculated using the thermoseed configurations arranged by doctors during preoperative planning in order to improve the accuracy and success rates of hyperthermic treatments.

2. Model

Conformal hyperthermia calculation methods primarily involve three numerical models, including the heat medium thermogenesis model, which determines the distribution of the instantaneous energy field during the treatment phase; the biological tissue heat transfer model, which determines the final distribution of the temperature field in the treatment region; and the tissue thermal damage model, which determines the effects of the treatment using specific treatment parameters.

2.1. Thermoseed thermogenesis model

In this study, a cylindrical nickel-copper alloy metal rod (Thermoseed) with a ferromagnet eddy current effect was implanted into tumor tissue for the numerical simulation analysis [13]. When the axial direction of a thermoseed is parallel to the direction of the magnetic field, the internal axial magnetic field of the medium satisfies the Helmholtz equation under scalar conditions. If the direction of the magnetic field is in the direction of the Z-axis, then the solution of the axial magnetic field can be obtained using the modified Bessel's equation with an order of zero (r, ϕ, z)

$$H_z = AI_0(\beta r) + BK_0(\beta r), 0 \leqslant r \leqslant a \tag{1}$$

$$\beta = [j\omega\mu(\sigma + j\omega\mu)] \tag{2}$$

In the content above, β is the propagation constant, A and B are constants which are decided by boundary conditions. The mathematical processes of the absorption power per unit length and radius of the thermoseed (a[m]), conductivity (σ[S/m]), permeability (μ[H/m]), frequency (ω[Hz]), and external magnetic field strength at the location of the medium (H_0[A/m]) was summarized by Haider [13] as follows.

$$P_{||} = \pi/\sigma |H_0|^2 g(x) x \tag{3}$$

We define that x is the magnetic induction of the implanted thermoseed

$$x = (\omega\mu\sigma)^{\frac{1}{2}} a, g(x) = Re\left\{\frac{xe^{j\pi/4}I_1(xe^{j\pi/4})}{I_0(xe^{j\pi/4})}\right\} \tag{4}$$

As shown in Eq. (3), the absorption power is proportional to the square of the magnetic field strength. By studying the relationship between the absorption power and the electromagnetic parameters of the medium, the absorption power was found to be the monotonically increasing function of the dielectric constant and magnetic field frequency, and proportional to the radius of the medium and the monotonically decreasing function of conductivity. Due to the complex expression of $g(x)$, a simple function was introduced to approximate $g(x)$.

$$g(x) = \begin{cases} 0.642 \times \frac{x^{3.437}}{1.917^{3.437} + x^{3.437}}, & \text{if } x \leqslant 20 \\ -0.0251 + 0.685 \left(\frac{0.825}{1 + e^{\frac{x-1.793}{-0.431}}} + \frac{1 - 0.825}{1 + e^{\frac{x-4.775}{-1.739}}} \right), & \text{else} \end{cases} \tag{5}$$

When calculating a single thermoseed, the value of $g(x)$ is negligible. However, the typical amount of thermoseed implanted in a tumor region during magnetic induction therapy ranges from one dozen to dozens. As the amount of thermoseed increases, the impact of $g(x)$ on the absorption power also increases. In this study, the effects of $g(x)$ on the absorption power during thermogenesis with multiple thermoseeds was considered during the construction of the thermoseed thermogenesis model, thereby increasing the accuracy of the calculation results.

Ferromagnetic alloy thermoseeds have Curie points, which typically range from approximately 50 to 80°C. Due to the Curie point effect, magnetic susceptibility decreases as temperature increases. In addition, the medium becomes changes from ferromagnetic to paramagnetic when the thermoseed temperature is approximate to the Curie point. The permeability, due to its relationship to magnetic susceptibility, also decreases significantly, resulting in a reduction in thermogenic power. Equation (6) displays the relationship between thermoseed permeability and temperature, where T_c represents the Curie point temperature of the thermoseed [14].

$$\frac{u}{u_{300K}} = \left(\frac{1}{1 + e^{[0.4(T - T_c) + 2]}} \right)^2 \tag{6}$$

2.2. Tissue heat transfer model

The tissue heat transfer model was established using Pennes perfusion tissue heat transfer model [15, 16]:

$$\rho c \frac{\partial T}{\partial t} = \nabla \cdot (k \nabla T) + w_b c_b (T_b - T) + q_m + q_r \tag{7}$$

In Eq. (7) [15–17], ρ represents the density of the biological tissue [kg/m^3]; c is the specific heat [J/(kg·K)]; T is the temperature [K], which is dependent on both time and position; t is time [s]; k is the thermal conductivity coefficient [W/(m·K)]; w_b is the blood perfusion rate [kg/(m^3·s)]; c_b is the specific heat of blood [J/(kg·K)]; and T_b is the temperature [K] of venous blood.

Several of the parameters in this equation could be affected by temperature changes. In order to improve the accuracy of the calculation results, the tissue thermal energy, heat transfer parameters of biological tissue, and effects of temperature changes on the blood perfusion rate were fully considered in this model. In addition, the specific heat capacity of water, variation coefficient of the tissue thermal conductivity, and variation coefficient of the blood perfusion rate were added to the model.

In the model, q_r was used to represent the external thermogenesis item $[W \cdot m^{-3}]$, and the heat transfer between the thermoseed and contact tissue was neglected in order to simplify the calculations. The thermoseed thermogenesis at time t was used to describe the heating process of tissue, and q_m

was used to represent the thermal energy $[W \cdot m^{-3}]$ converted from biochemical energy due to local metabolism. q_m can be described as [17]

$$q_m = q_{m0} \cdot \emptyset^{\frac{T-37}{10}} \tag{8}$$

where q_{m0} is the reference metabolic rate at a body temperature of 37°C and the typical value of ϕ is equal to 3.0 [17].

According to the law proposed by Müller [18] and Zhai et al. [19], the heat transfer parameters of biological tissue associated with tissue temperature can be expressed by the following.

$$\begin{cases} c\left(T\right) = 4190\left(0.37 + 0.63 l_c \omega\right) \\ k\left(T\right) = 0.419\left(0.133 + 1.36 l_k \omega\right) \end{cases} \tag{9}$$

T is the tissue temperature. ω is the water content of the tissue, which varies based on the tissue type. For example, the water content of liver tissue is approxitely 0.69 [18]. l_c and l_k represent the variation coefficients of the specific heat capacity of water and the tissue thermal conductivity over changes in temperature.

$$\begin{cases} l_c = 1 + 1.016 \times 10^{-4}\left(T - 20°C\right) \\ l_k = 1 + 1.78 \times 10^{-3}\left(T - 20°C\right) \end{cases} \tag{10}$$

During magnetic induction hyperthermia, an increase in tissue temperature can induce vascular expansion and, thereby, accelerate blood flow and lead to a change in blood perfusion rate. The condition can be described quantitatively by [20]

$$\omega_b\left(T, \Omega\right) = \omega_{b0} f_T f_u \tag{11}$$

where ω_{b0} represents the blood perfusion rate under homeostasis, and f_T represents the correlation coefficient of the blood perfusion rate and tissue temperature, which is expressed as

$$f_T = \begin{cases} 4 + 0.6\left(T - 42\right), & \text{if } 37°C \leqslant T \leqslant 42°C \text{ and } \Omega < 1 \\ 4, & \text{if } T > 42°C \text{ and } \Omega < 1 \\ 0, & \text{if } \Omega > 1 \end{cases} \tag{12}$$

where f_u represents the tissue intact coefficient, expressed as [21]

$$f_u = \exp\left(-\Omega\right) \tag{13}$$

In Eq. (13), Ω refers to the damage function of biological tissue during hyperthermia; this value can be calculated with the Arrhenius biological thermal damage equation.

2.3. Tissue thermal damage model

In the current clinical applications of magnetic induction hyperthermia, biological tissue temperature is usually used to indirectly assess the extent of tissue thermal damage without direct quantitative dose standards. Thus, in this paper, a tissue thermal damage model was introduced and a quantitative description of biological tissue thermal damage was conducted in order to improve magnetic induction treatment efficacy assessments.

According to a study conducted by He and Bischof et al., biological tissue thermal damage is not only related to tissue temperature, but also by the duration of exposure to certain temperatures. When tissue

cells are exposed to an environment with a temperature of $T(t)$, the survival rate (f_u) can be calculated using Eq. (13), and the cumulative tissue damage and necrotic area can be estimated as

$$\Omega = \int_0^\tau k_c dt \tag{14}$$

where τ is the total treatment time, and k_c is the cell loss rate, expressed with the Arrhenius model as [22]

$$k_c = A_c \exp\left(-\frac{\Delta E_c}{RT}\right) \tag{15}$$

where A_c is the frequency factor, ΔE_c indicates the activation energy, and R represents the universal gas constant. The mathematical relationship between ΔE_c and A_c was summarized by He and Bischof et al. [21,23] as

$$\ln(A_c) = 0.38 \times \frac{\Delta E_c}{10^3} - 9.36 \tag{16}$$

If $A_c = 4.362 \times 10^{43} s^{-1}$ and $\Delta E = 287.49 \times 10^3 \text{J} \cdot \text{mol}^{-1}$ are the thermal damage parameters, then the selected evaluation function,

$$\eta = (1 - f_u) \times 100\% \tag{17}$$

indicates the extent of thermal damage in the cells. According to relevant theories and experiments, thermal damage is irreversible, and cells are considered to be thermally damaged when Ω is greater than 1 and 63% or more of the tissue is thermally damaged. These values were chosen as criteria in this paper since, if Ω is greater than 1, irreversible damage will occur in the normal tissue, resulting in discomfort.

3. Numerical techniques based on FVM

In order to predict the temperature distributions of magnetic induction therapy conformal hyperthermia, the bio-heat transfer Pennes Eq. (7) must be solved and information regarding the dynamic temperature spread of the treatment region must be obtained. The existing methods used to solve this equation include mathematical analysis methods and computer numerical methods. Computer numerical method solutions are exact and more intuitive, but not applicable to the practical applications of clinical computing software. Mathematical analysis methods have been widely applied to computer software. Using FVM, Eq. (7) was discretized and solved, and the computational node temperature was obtained.

The 3D computational space was discretized as a regular cuboid infinitesimal, and the 3D Pennes governing Eq. (7) was integrated within a controlled volume [24]:

$$\int_t^{t+\Delta t} \int_{\Delta V} \rho c \frac{\partial T}{\partial t} dV dt = \int_t^{t+\Delta t} \int_{\Delta V} k \left(\frac{\partial^2 T}{\partial x^2} + \frac{\partial^2 T}{\partial y^2} + \frac{\partial^2 T}{\partial z^2}\right) dV dt +$$
$$\int_t^{t+\Delta t} \int_{\Delta V} w_b c_b (T_b - T) dV dt + \tag{18}$$
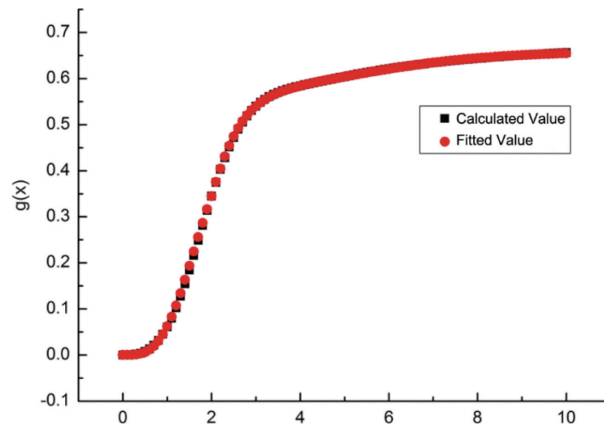$$\int_t^{t+\Delta t} \int_{\Delta V} (q_m + q_r) dV dt$$

Fig. 1. Simplified fitting model of $g(x)$.

For a uniform grid system, Eq. (18) can be transferred according to the Ostrogradskee integral equation as

$$\frac{\rho c}{\Delta t}\left(T_P - T_P^t\right)\Delta V = k_e A_e \frac{T_E - T_p}{\Delta x} - k_w A_w \frac{T_P - T_W}{\Delta x}$$

$$+ k_n A_n \frac{T_N - T_P}{\Delta y} - k_w A_w \frac{T_P - T_W}{\Delta y} \tag{19}$$

$$+ k_t A_t \frac{T_T - T_P}{\Delta z} - k_b A_b \frac{T_P - T_B}{\Delta z}$$

$$+ w_b c_b \left(T_b - T_P\right)\Delta V + \left(q_m^t + q_r^t\right)\Delta V$$

In this equation, T_P and T_P^t represent the temperatures at time points (x, y, z) of $t + \Delta t$, t, A_τ represents the area of surface τ (integral direction) of the control volume, and ΔV represents the volume of the control volume. If $h_i = \frac{k_i A_i}{\delta_{IP}}$, $(i = w, e, s, n, b, t)$ then Eq. (19) can be simplified as

$$\begin{cases} h_p T_p = h_w T_w + h_e T_e + h_s T_s + h_n T_N + h_b T_B + h_t T_T + h_p^t T_P^t + \lambda \\ h_p^t = \frac{\rho c}{\Delta t} \\ \lambda = (w_b c_b T_b + q_m^t + q_r^t)\Delta V \\ h_p = h_w + h_e + h_s + h_n + h_b + h_t - \zeta \\ \zeta = -w_b c_b \Delta V \end{cases} \tag{20}$$

Due to its high efficiency and calculation storage space, the tri-diagonal matrix (TDMA) algorithm was used to solve the discrete Eq. (20) resulting from the FVM, and the generic solutions for the temperatures of each node were obtained.

4. Numerical simulation and validation

4.1. Experimental objectives

Conduct an agar phantom experiment in order to measure the heating of multiple thermoseeds in an agar phantom. Using computer simulations, validate the accuracy and reliability of the resulting models and numerical methods by comparing the simulation results to the measured values.

Table 1
Agar phantom thermos-physical properties

No	Temperature/°C	Thermal conductivity/($W \cdot m^{-1} \cdot K^{-1}$)	Thermal diffusivity/($\times 10^7\ m^2 \cdot s^{-1}$)
1	20.0 ± 0.1	0.2176 ± 0.0026	0.8838 ± 0.0044
2	20.1 ± 0.1	0.2077 ± 0.0024	0.8853 ± 0.0047

Fig. 2. Magnetic induction hyperthermia system (MIH-100).
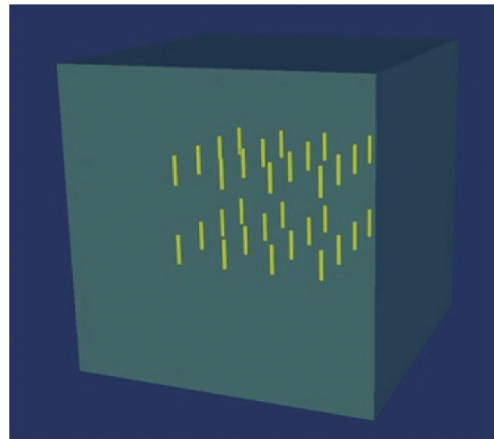

Fig. 3. Mathematical model of the 32 thermoseeds implanted into the phantom.

4.2. Experimental apparatus

4.2.1. Agar phantom

In this paper, an agar phantom was used to validate the numerical model under laboratory conditions. The proportioning ratio was as follows: 400 g weighed purified agar powder, 2.4 g sodium chloride, and 1 g sodium nitride. The agar mixture was stirred and dissolved in 10 L distilled water and placed in a microwave oven and heated for 15 minutes to approximately 95°C. The solution was extracted several times during the heating process and stirred to ensure even dissolution. The heating process was completed when the solution was gel-like; then, the solution was cooled naturally to approximately 50°C. The solution was uniformly perfused in 60 mm × 60 mm × 60 mm molds and cooled in room temperature for 24 hours. The cubic experimental models were formed. The methods frequently used to measure the thermo-physical properties of prepared agar phantoms include the Transient Plane Source Method and the harmonic technique (3-omega) [25], The harmonic technique was used for the purposes of this study. The 3-omega thermo-physical property test system from the University of Chinese Academy of Sciences was used as the measuring instrument. The measurement results are shown in Table 1.

4.2.2. Magnetic induction hyperthermia system (MIH-100)

This alternating magnetic field device was jointly developed by the new medical technology lab at Tsinghua University and Fuzhou Haolian Medical Technology Co., Ltd. (see details in Fig. 2). The device parameters are given in Table 2.

4.2.3. The ferromagnetic thermoseed used in this study was a medical Ni-Cu alloy thermoseed

The key parameters are given in Table 3 [14,26]. The thermoseed was implanted with puncture needles and cannulas.

Table 2
MIH-100 parameters

Parameter	Unit	Value
Magnetic field intensity	kA · m^{-1}	9.6
Magnetic field frequency	kHz	116
Magnetic field direction	–	Parallel to z axis

Table 3
Medical Ni-Cu thermoseed parameters

Parameter	Unit	Value
Length	mm	6.0 ± 0.1
Diameter	mm	0.80 ± 0.02
Mass	mg	25.0 ± 0.1
Density	kg $\cdot m^{-3}$	8908 ± 100
Electrical conductivity	$S \cdot m^{-1}$	(2.30 ± 0.08)
Curie point	°C	60–83[①]
Specific heat capacity	$J \cdot kg^{-1} \cdot °C^{-1}$	439 ± 20

[①]Different thermoseed curie points should be used based on clinical request.

4.2.4. Measuring tools

Measuring thermocouples, multi-channel temperature recorder and vernier caliper.

4.3. Experimental subjects

Cubic agar phantom. Thirty-two thermoseeds were implanted uniformly in two rows according to the mathematical model shown in Fig. 3. The Curie point temperature of the thermoseed was equal to 77°C. The operation was conducted at room temperature.

4.4. Temperature measurement locations

10 mm in front of the center of the phantom, 14.14 mm to the right of the center of the phantom, 10 mm to the left of the center of the phantom, center of the phantom, 10 mm to the right of the center of the phantom, and 10 mm behind the center of the phantom.

4.5. Experimental procedures

4.5.1. Preparation of agar phantom

The cubic agar phantom was prepared according to the method mentioned previously. Then, the phantom was placed under a constant temperature of 24°C for 24 hours in order to achieve balance with the external environment.

4.5.2. The position markers, thermoseed, and thermocouples were implanted

The spatial coordinates of the thermoseed and the various temperature measurement points were calculated, and the surface of the agar phantom was marked. Then, the implantation depth of the thermocouples were marked, and puncture needles and trocar used to puncture the agar phantom according to the position of each point in order to ensure proper placement of the implants. Templates were used to implant the thermoseed and thermocouples in the specified locations. The puncture needles were rotated and inserted slowly to the specified locations durin ghte operation in order to ensure perpendicular insertion.

4.5.3. Heating experiments

An insulation board was placed beneath the underside of the phantom after implantation. Then, the phantom was placed between the magnetic poles of the experimental equipment, and the temperature of each point in the phantom was monitored for five to ten minutes. When the temperature of each point was not significantly different from the temperature of the external environment, the magnetic field parameters were set, the experimental equipment was initiated, and the thermoseed heating experiment was conducted until the heating curves plateaued.

4.5.4. Repeated experiments

After the first experiment, the phantom was allowed to cool to its initial temperature. Then, the heating experiment was replicated five times.

4.5.5. Experimental data processing

The results of the five experiments were compared. The mean values of the three experiments with approximate results were used to draw the final heating curve. Then, the phantom was cut, and the positions of the thermoseeds and measurement points were observed in order to determine whether they were consistent with the experimental design. Once significant deviation occurred, another phantom was prepared, and the experiment was replicated.

4.5.6. Calculation verification

The simulation was performed using the mathematical model shown in Fig. 2. In order to ensure accuracy, a 3D discrete calculation with a step-length of 1 mm was selected, and the calculated temperature value of each temperature measurement point was output. Then, the results were compared to the experimental results.

As shown in Fig. 4, the curve was plotted with the calculated values after correcting the temperature differences with the mean temperature value of the experiment. When the magnetic field parameter was large enough, the temperature distribution of the warmed ferromagnetic thermoseed plateaued with self-regulation. In addition, the calculated and measured temperatures were different. This could have resulted from slight deviations in the spatial locations or the effects of the slight angle between the thermoseed and magnetic field on the thermogenesis power since precisely positioning the thermoseed during the implantation process is difficult. It could have also been the result of insufficiently precise thermocouple implantation, leading to the offset of the actual measurement points and inconsistencies in the calculated values.

Despite the effects of these manual errors, the errors between the calculated values and measured values at each measurement point were within the allotted range ($\pm$ 0.5°C). Thus, the mathematical model and numerical computations were reliable.

5. Applications

During magnetic induction hyperthermia, preoperative CT scans must be conducted, and the results must be scanned to the planning system. The GPU real-time volume rendering method is applied to display the 3D anatomical structures of the patient on the surgical planning interface. Subsequently, the tumor tissue is divided by manually sketching the tissue outlines or with the semi-automatic segmentation algorithm in order to establish a 3D surface model and determine the boundary conditions. Then, conformal thermoseed implantation is conducted on the tumor tissue alternately according to the template size,
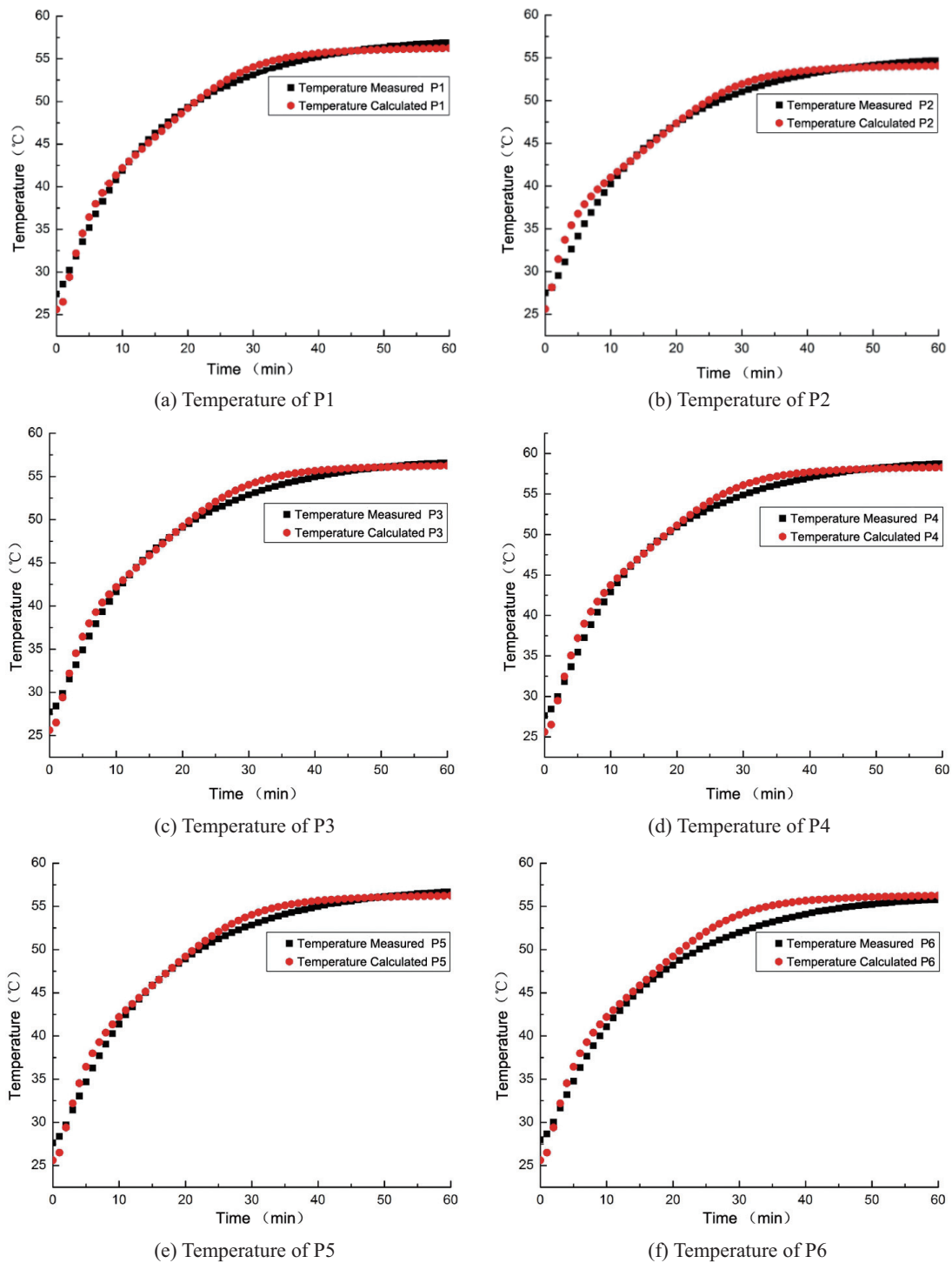
(a) Temperature of P1

(b) Temperature of P2

(c) Temperature of P3

(d) Temperature of P4

(e) Temperature of P5

(f) Temperature of P6

Fig. 4. Temperatures of the 6 temperature measuring points over time.

Table 4
The bio-heat transfer parameters of human tissue

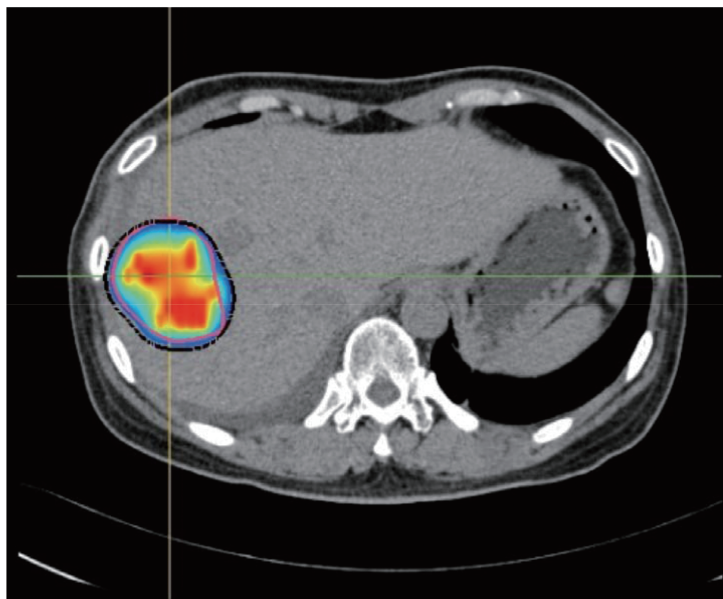| Tissue	Density $\rho/(\mathrm{kg} \cdot m^{-3})$	Specific heat capacity $c/(J \cdot \mathrm{kg}^{-1} \cdot {}^{\circ}\mathrm{C}^{-1})$	Thermal conductivity $k/(W \cdot m^{-1} \cdot {}^{\circ}\mathrm{C}^{-1})$	blood perfusion rate $w_b/(\mathrm{kg} \cdot \mathrm{m}^{-3} \cdot s^{-1})$
Air	1.29	10000	0.024	0
Skin	1100	3700	0.370	0.012
Fat	1100	4483	0.204	0.231
Muscle	1040	3500	0.518	0.028
Skeleton	1600	2000	0.3	0.154
Liver	1040	3500	0.518	2.631
Spine	1600	2000	0.3	2.336
Tumor	1050	3639	0.560	0.50
Blood	1060	3770	–	–

Fig. 5. Example calculation of the temperature field distribution using the magnetic induction therapy conformal hyperthermia plan.

and the surgeons add and adjust the surgical routes, tissue parameters, magnetic field parameters, and treatment times. Next, the system reconstructs the damaged area and displays the anatomical structure of the patient after integration according to the thermoseed distribution of the targeted region. The doctors can then compare this damaged area to the tumor region in order to determine whether the surgical plan is capable of effectively inactivating the tumor.

In the example calculation in Fig. 5, the red curve indicates the tumor; the black curve indicates the outermost thermal damage; the colored area is the temperature field distribution; and the outermost blue area is an isotherm at 48°C. Refer to the study conducted by Holmes [27] and Deng Zhongshan [28] et al. for the bio-heat transfer parameters of human tissue; the details are shown in Table 4.

During clinical operations, doctors use puncture needles to implant thermoseeds into patients according to the needle insertion points, insertion angles, and depths planned during the thermoseed implantation paths before surgery. Then, the hyperthermia operations are performed according to preset magnetic field frequencies, intensities, and treatment times. In general, since inserting the needle into the intended

site is difficult, real-time ultrasound imaging is required for guidance and confirmation of the specific location of the surgical instrument. In addition, iron constantan thermocoupling is used to measure the tissue temperature during the surgical procedure.

6. Conclusions

In this study, a thermoseed thermogenesis model, tissue heat transfer model, and tissue thermal damage model were established based on target region temperatures and thermal damage distributions during the preoperative treatment planning system of magnetic induction hyperthermia. The contribution of $g(x)$ to the thermoseed absorption power was considered in the thermoseed thermogenesis model since, during an actual magnetic induction treatment, the typical amount of thermoseed implanted in the tumor region ranges from one dozen to dozens, and the accurate calculation of $g(x)$ can improve the accuracy of the temperature distribution calculation result. In the tissue heat transfer model, the effects of temperature changes on several calculation parameters were considered in order to further improve the accuracy of the temperature distribution calculation results. The tissue thermal damage model quantitatively described the thermal damage field and accurately evaluated the therapeutic effects.

Using FVM, the numerical solution methods were also studied in this paper. Phantom human model experiments and computer numerical simulations were designed, and the accuracy and reliability of the 3D magnetic induction hyperthermia models and their corresponding numerical computational methods were verified. The results were applied to magnetic induction hyperthermia planning system software. The 3D models established in this paper, as well as their corresponding numerical computation methods, provided accurate temperature and thermal damage distributions in the targeted regions..

In actual clinical trials, large vessels could be present in the region undergoing hyperthermia treatments. Thus, the impact of blood flow velocity should be considered in the calculations conducted in this paper. The accurate prediction of thermal fields and damaged fields in vascular areas require further studies.

Acknowledgements

References

[1] Gilchrist R K, Medal R, Shorey W D, et al. Selective inductive heating of lymph nodes [J]. Ann Surg, 1957, 146(4): 596-606.

[2] Guy A W. Electromagnetic fields and relative heating patterns due to a rectangular aperture source in direct contact with bilayered biological tissue [J]. Microwave Theory and Techniques, IEEE Transactions on, 1971, 16(2): 214-223.

[3] Kritikos H N, Foster K R, Schwan H P. Effect of Surface Cooling and Blood Flow on the Electromagnetic Heating of Tissue[C]//Microwave Symposium Digest, 1977 IEEE MTT-S International. IEEE, 1977: 354-356.

[4] Van de Kamer J B, De Leeuw A A C, Hornsleth S N, et al. Development of a regional hyperthermia treatment planning system [J]. International Journal of Hyperthermia, 2001, 17(3): 207-220.

[5] Chin R B, Stauffer P R. Treatment planning for ferromagnetic seed heating. International Journal of Radiation Oncology* Biology* Physics, 1991, 21(2): 431-439.

[6] Jordan A, Scholz R, Wust P, et al. Magnetic fluid hyperthermia (MFH): Cancer treatment with AC magnetic field induced excitation of biocompatible superparamagnetic nanoparticles. Journal of Magnetism and Magnetic Materials, 1999, 201(1): 413-419.

[7] Johannsen M, Gneveckow U, Thiesen B, et al. Thermotherapy of prostate cancer using magnetic nanoparticles: feasibility, imaging, and three-dimensional temperature distribution. European Urology, 2007, 52(6): 1653-1662.

[8] Gneveckow U, Jordan A, Scholz R, et al. 3-Dimential calculation of the temperature distribution during thermotherapy with magnetic nanoparticles. Proceedings of the 23rd ESHO Meeting Berlin, Berlin, 2006. 51-51.

[9] Linthorst M, Drizdal T, Joosten H, et al. Procedure for creating a three-dimensional (3D) model for superficial hyperthermia treatment planning [J]. Strahlentherapie und Onkologie, 2011, 187(12): 835-841.

[10] Di Barba P, Dughiero F, Sieni E. Field synthesis for the optimal treatment planning in Magnetic Fluid Hyperthermia [J]. Archives of Electrical Engineering, 2012, 61(1): 57-67.

[11] Paulides M M, Stauffer P R, Neufeld E, et al. Simulation techniques in hyperthermia treatment planning [J]. International Journal of Hyperthermia, 2013, 29(4): 346-357.

[12] Stigliano R V. Development and validation of a treatment planning model for magnetic nanoparticle hyperthermia cancer therapy [D]. Dartmouth College, 2014.

[13] Haider S A, Cetas T, Wait J, et al. Power absorption in ferromagnetic implants from radiofrequency magnetic fields and the problem of optimization. IEEE Transactions on Microwave Theory and Techniques, 1991, 39(11): 1817-1827.

[14] Cai Dongyang, Cao Xinrong, Zhuo Zihan, et al. Analysis and experimental verification of the heat generation by an implanted thermoseed in magnetic induction hyperthermia(in Chinese). Journal of Tsinghua University (Science and Technology), 2012, 52(12): 1741-1745.

[15] Pennes H H. Analysis of tissue and arterial blood temperatures in the resting human forearm. Journal of Applied Physiology, 1948, 1(2): 93-122.

[16] Pennes H H. Analysis of tissue and arterial blood temperatures in the resting human forearm. Journal of Applied Physiology, 1998, 85(1): 5-34.

[17] Liu J, Deng Z S. Physics of tumor hyperthermia [M]. 2008.

[18] Müller G J, Roggan A. Laser induced interstitial thermotherapy. Bellingham: SPIE Press, 1995.

[19] Zhai W, Xu J, Zhao Y, et al. Preoperative surgery planning for percutaneous hepatic microwave ablation. Proceedings of Medical Image Computing and Computer-Assisted Intervention – MICCAI 2008. New York: Springer Berlin Heidelberg, 2008: 569-577.

[20] Jiang S, Zhang X. Effects of dynamic changes of tissue properties during laser-induced interstitial thermotherapy (LITT). Lasers in Medical Science, 2005, 19(4): 197-202.

[21] He X, Bischof J C. The kinetics of thermal injury in human renal carcinoma cells. Annals of Biomedical Engineering, 2005, 33(4): 502-510.

[22] Bhowmick S, Swanlund D J, Bischof J C. Supraphysiological thermal injury in Dunning AT-1 prostate tumor cells. Journal of Biomechanical Engineering, 2000, 122(1): 51-59.

[23] He X, Bischof J C. Quantification of temperature and injury response in thermal therapy and cryosurgery. Critical Reviews in Biomedical Engineering, 2003, 31(5&6).

[24] LI Renxian. The Basis of Finite Volume Method [M]. Beijing: National Defence Industry Press, 2005: 102-130.

[25] Hasegawa Y, Murata M, Tsunemi F, et al. Thermal Conductivity of an Individual Bismuth Nanowire Covered with a Quartz Template Using a 3-Omega Technique. Journal of Electronic Materials, 2013, 42(7): 2048-2055.

[26] CAI Dongyang, LI Li, KONG Weichao et al. Feasibility of the Magnetic Induction Hyperthermia Combined with 125I Brachytherapy(in Chinese). Science & Technology Review, 2013, 31(001): 18-22.

[27] Holmes K. Biological structures and heat transfer. Proceedings of Allerton Workshop on the Future of Biothermal Engineering, 1997.

[28] Deng Zhongshan, Liu Jing. Study on the Noninvasive Measurement on the Biological Blood Perfusion in Vivo (in Chinese). Chinese Journal of Biomedical Engineering, 2001, 20(1): 1-11.